ARTICLE

OPEN

Check for updates

Adjoint tomography of the Italian lithosphere

Federica Magnoni [1✉], Emanuele Casarotti[1], Dimitri Komatitsch[2], Raffaele Di Stefano [1], Maria Grazia Ciaccio [1], Carl Tape [3], Daniele Melini [1], Alberto Michelini [1], Antonio Piersanti[1] & Jeroen Tromp [4]

The evolution and state of geological structure at Earth's surface is best understood with an accurate characterization of the subsurface. Here we present seismic tomographic images of the Italian lithosphere based on ground motion recordings and characterized by compressional and shear wavespeed structure at remarkable resolution, corresponding to a minimum period of ~10 s. Enhanced accuracy is enabled by state-of-the-art three-dimensional wavefield simulations in combination with an adjoint-state method. We focus on three primary findings of our model *Im25*. It highlights the distribution of fluids and gas (CO_2) within the Italian subsurface and their correlation with seismicity. It illuminates Mt. Etna volcano and supports the hypothesis of a deep reservoir (~30 km) feeding a shallower magma-filled intrusive body. Offshore of the eastern Italian coast, it reveals that the Adriatic plate is made of two distinct microplates, separated by the Gargano deformation zone, indicating a complex lithosphere and tectonic evolution.

[1] Istituto Nazionale di Geofisica e Vulcanologia (INGV), Rome, Italy. [2] CNRS Laboratory of Mechanics and Acoustics, Marseille, France. [3] University of Alaska Fairbanks, Fairbanks, AK, USA. [4] Princeton University, Princeton, NJ, USA. ✉email: federica.magnoni@ingv.it

The Italian peninsula is characterized by heterogeneous geological structures resulting from a complex tectonic evolution featuring the Tyrrhenian, Adriatic, and European plates[1–3] (Fig. 1). The relationships among the three plates change along the peninsula and reflect episodes of mountain building, subduction, continental collision, slab roll-back, and back-arc basin formation. The two main mountain belts—the Alps and Apennines—have different but connected origins. A large sedimentary basin dominates the area of the Po Plain in northern Italy, with sediments up to 8 km thick[4]. Other smaller but significant basins in Central Italy have developed as part of the extensional regime orthogonal to the Apennines chain and in the Tyrrhenian back-arc. Campi Flegrei, Vesuvio, Mt. Etna volcano, and the Eolian arc are broad volcanic regions whose magmatic systems are not fully understood. Two seamounts, Marsilii and Vavilov, are the main volcanoes of an extensive magmatic province related to the spreading center of the southern Tyrrhenian Sea.

The Adriatic plate is peculiar for representing the foreland of two non-coeval mountain ranges: the Apennines to the west and the Dinarides-Hellenides to the east[5]. The bathymetry of the Adriatic plate is shallow in the northern part, from Istria to the Gargano promontory, and suddenly deeper in the south toward the Ionian Sea. The tectonic structure of the Adriatic plate is debated[6]. It has been considered either as an Africa promontory involved in the African–European plate collision or as an independent block separated from Africa by the Ionian oceanic crust since Mesozoic or Permian times ([6,7], and references therein). More recent seismic and GPS data corroborate a hypothesis that the Adriatic lithosphere behaves as two separate microplate blocks[6,8].

Despite the important role of the Adriatic plate in the geodynamics of the central Mediterranean, its lithospheric structure, at least in terms of V_p and V_s profiles, is poorly known due to a lack of seismic stations, poor earthquake location quality (large observational gaps), and the consequent lack of coverage by classical seismic tomography methods. Most of the literature is limited to continental-scale tomography (e.g.,[9–12]), often with low vertical resolution and sparse node density (e.g.,[13,14]). Similarly, the lithosphere of the southern Tyrrhenian Sea, northwest of the Calabrian subduction zone, is poorly constrained in terms of both V_p and V_s from previous tomographic studies due to limited ray coverage[15] or low resolution (e.g.,[9,11,16]). Interesting results for the Tyrrhenian basin can be found in[17] but limited to a V_s
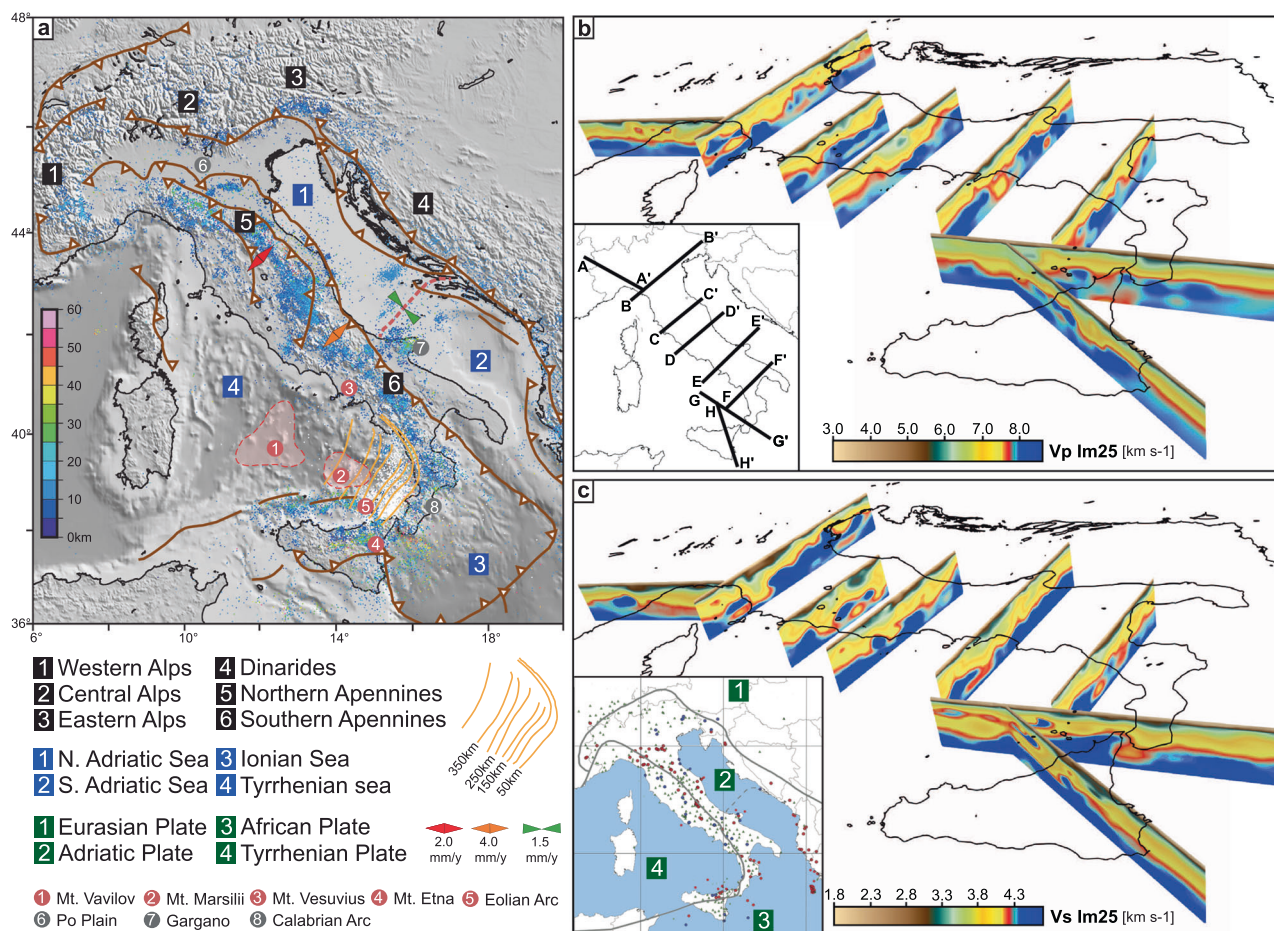
Fig. 1 Tectonic setting of Italy and vertical cross-sections of model *Im25*. **a** Map of the main tectonic and structural features of the Italian region (modified after[3]); deformation rates[6] are denoted by colored arrows (see legend). Relocated seismicity from the Italian Bulletin of INGV[85] is represented by the dots, colored by earthquake depth. Isolines indicate the deepening of the Ionian slab[86]. The light red areas indicate volcanic provinces. **b** Vertical sections of the *Im25* V_p model visualized in 3D; coastlines are plotted on top of the slices. See inset for a map view. **c** Corresponding vertical sections for the *Im25* V_s model. The inset shows earthquakes (dots) and stations (triangles) used in this study. Red dots are the 123 events considered for the first 12 iterations, blue dots denote 40 events added at the 13th iteration. Grey lines indicate a schematic representation of plate boundaries at Moho depth (modified after[6,29,87,88]). The dashed line in the Adriatic Sea represents the theoretical separation between the two microplates that compose the Adriatic plate[6].

lithospheric model, or in[18] for V_p and V_s but investigating a more local structure and at greater depths.

Most available models of the Italian wavespeed structure based on body- or surface-wave tomography are either high resolution but limited to shallow crustal depths and restricted areas of interest (e.g.,[19–24]) or are at continental (European or Mediterranean) scales, capturing gross mantle features but missing finer Italian lithospheric details (e.g.,[13,25–27]). Other tomographic studies have focused on the entire Italian region but usually constrain only one wavespeed parameter (V_p or V_s) or are at lower resolution (e.g.,[15,28,29]). Independent shear-wavespeed models have been also retrieved from ambient noise data, and they are able to constrain V_s with a uniform coverage, but techniques, dataset, and resolution are different (e.g., at local/regional scale[30–35]). Full waveform adjoint tomography models are presently available for the European continent, offering large-scale hints on the Italian lithospheric structure inferred from wavespeed values in the shallow layers of their models[9,11,12,36].

In the last two decades, a large number of high-quality, three-component seismic instruments have been deployed in Italy[37], and several moderate seismic sequences have been recorded. These data represent an invaluable source of information to construct, for the first time, a comprehensive 3D wavespeed model of the Italian lithosphere based on full waveform adjoint tomography ([38], and references therein).

Recent studies demonstrate the success of the adjoint-state method[39,40] in imaging complex structures in many regions in the world (e.g.,[11,16,36,41–47]) and on a global scale[48,49]. The main advantages of the method are a) comparing entire seismic traces simulated for realistic 3D Earth models to corresponding recorded waveforms and b) performing inversions constrained by all the phases that appear in these seismograms.

Here we present a new 3D tomographic model obtained by applying the method to the entire Italy. We start from a recent 3D traveltime tomographic model for the peninsula[29] and increase its resolution by taking advantage of a full waveform extended dataset (Fig. 1). We perform high-frequency wavefield simulations using a spectral-element method (SEM), implemented by the code SPECFEM3D_Cartesian[50], and we exploit the SEM accuracy within the adjoint-state method to perform a 3D tomographic iterative inversion using full waveforms (Section "Forward and inverse modeling").

Our objectives are to better image the lithospheric structure of the Italian region, both inland and as far offshore as possible, and to extend our analyses to presently poorly known or unconstrained areas of the peninsula, such as the Adriatic Sea and the southern Tyrrhenian Sea. We analyze features along sections that have been considered in the literature[29] and cross meaningful tectonic/seismological structures. We also present cross-sections through previously poorly resolved areas where our model offers new insights.

Results

Successive iterations of the adjoint tomographic inversion gradually improve the starting tomographic model[29] while reducing the value of the misfit function chosen to assess differences between observed and simulated seismic wavefields. After 25 iterations we obtain our final model of the Italian lithosphere, *Im25*. It confirms some strong features characterizing this region, and it also reveals new interesting structures that contribute to our understanding of the complex tectonic setting of Italy.

Misfit behavior and waveform fit. A single evaluation of the misfit function considers an input tomographic model as well as waveform differences within thousands of measured time windows (Section "Forward and inverse modeling"). Trends of the misfit function evaluations are summarized in Supplementary Fig. 1a. The first point of the red curve in the figure represents the misfit function value of the initial model *Im00* (after a first source inversion, Section "Source inversion"). The tomographic inversion progressively reduces the value of the misfit function (Supplementary Figs. 1a, b) pointing at improved modeling of the recorded seismograms and corresponding enhanced imaging of Earth structure.

An example of how synthetic seismograms improve over the course of iterations is shown in Supplementary Fig. 2. Quantitative comparisons of waveforms show how successive model iterations result in synthetic seismograms that better reproduce the recorded data for phase arrivals, amplitude, and duration. The tomographic iterations mainly adjust the phase of the synthetics due to the chosen misfit function (Section "Forward and inverse modeling"), yet entire seismograms are affected, resulting in an adjustment of the amplitudes as well. Some features of the seismograms are still not matched by our final model *Im25*, suggesting that future extensions of this work will need to add more data, perform some more iterations, and/or invert for additional model parameters, such as transverse anisotropy or attenuation. Nevertheless, the present model is able to reproduce many of the main features of the observed seismograms, which supports the robustness of the imaged structures.

An independent test of the improved quality of fit for *Im25* has been carried out by[51], using the 2016, M_w 6.0 Amatrice earthquake, which was not included in our dataset.

Tomographic model. In order to provide a general overview of model *Im25*, we analyze it in the same seven cross-sections chosen by[29] and one section through Mt. Etna volcano (Figs. 1b, c, 2, 3, Supplementary Figs. 3–5). Then we focus on the complex zone of the Adriatic Sea (Figs. 4, 5, Supplementary Figs. 6–10), where insights come from recent geological and geodetic studies[6,8] but where high-resolution 3D regional tomographic models were not available. These comparisons highlight the features that are better constrained or new in our model *Im25*.

The well known tectonic structures of the initial 3D V_p model are more clearly revealed in *Im25* V_s profiles, such as the high-V_p body in northwestern Italy known as the Ivrea Verbano body (down to ~20–30 km depth). This is a robust feature in previous tomographic models of the region, also obtained with different techniques, such as those using ambient noise and/or earthquake-based methods (e.g.,[33–35]). This feature is stable in our V_p *Im25* model with respect to *Im00*, and now reveals corresponding deepening low-V_s values (section AA' in Supplementary Fig. 4). Another example is the under-thrusting of the Adriatic crust below the Tyrrhenian crust, which is evidenced by lower V_p and now also V_s values deepening southwestward along the peninsula and by low wavespeeds related to the asthenospheric wedge (sections CC', DD', and EE' in Fig. 2, BB' and FF' in Supplementary Figs. 4, 5).

New interesting features are highlighted in all cross-sections, particularly considering the results for V_s and the V_p/V_s ratio. For the sections in Central Italy (Fig. 2), by exploiting the connections between these parameters and the presence of fluids and gas (e.g.,[52]), our full waveform tomography reveals features in agreement with recent geochemical and seismotectonic studies on fluid and gas (CO_2) distribution within the subsurface[23,53].

Model *Im25* provides high-resolution images of the area around the Mt. Etna volcano (Fig. 3), extending further and deeper the interpretation of previous findings (e.g.,[54]), in agreement with recent seismological, petrological, and volcanological studies[54–56].
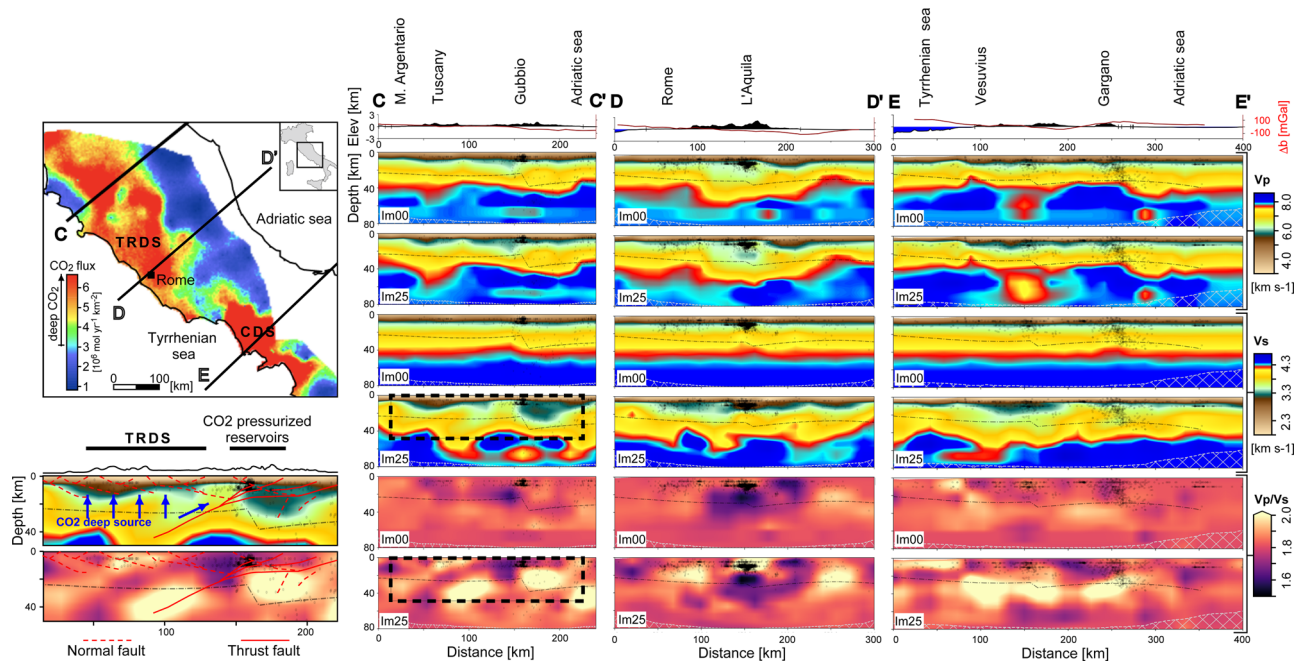
Fig. 2 Detailed vertical cross-sections of models *Im00* and *Im25* for sections CC', DD', EE', and comparison with CO_2 degassing areas. For each section we show surface topography and Bouguer anomalies (top), and V_p, V_s, and the V_p/V_s ratio for models *Im00* and *Im25*. Dotted black lines in each section represent the Moho[29]. White dashed areas are not well-resolved in *Im25* model. Black dots represent relocated seismicity from the Italian Bulletin of INGV[85]. The map (modified after[58]) represents the degassing of CO_2 from deep sources; TRDS is the Tuscan-Roman degassing structure and CDS is the Campanian degassing structure. The sections below show a close-up of section CC' for V_s and V_p/V_s in *Im25* model within the boxes highlighted in the sections CC' (black dashed contours). The superimposed traces are structural features[58].

The sections of *Im25* cutting through South Italy (Fig. 3, Supplementary Fig. 5) image strong wavespeed contrasts and sharp geometries in the subduction zone of the Calabrian Arc. These show the relationship between the Tyrrhenian plate and the northwestward subducting Ionian plate (almost sub-horizontal above 60 km depth; e.g.,[18], and references therein) and illuminate the volcanic region from the Marsilii Seamount spreading center to Mt. Etna.

The results of model *Im25* play also an important role in the debate about the structure and behavior of the Adriatic plate (Figs. 4, 5, Supplementary Figs. 6–10). This could also explain the uneven distribution of the Adriatic seismicity and the differences in the observed stress regimes.

An evidence of the robustness and reliability of our *Im25* model results from the agreement in the comparisons of V_s profiles extracted at selected stations from our model and studies using different techniques, dataset, and regions (Supplementary Fig. 11).

Horizontal cross-sections provide complementary views of our tomographic model (Supplementary Figs. 3g, h). Variations in V_p and V_s are generally negative (i.e., the new wavespeed is lower than the initial one) along the continent and positive along marine areas. In both sub-figures—but especially for V_s—the footprint of the large sedimentary basin of the Po Valley is highlighted by a wide zone of lower wavespeeds in northern Italy. The variations of V_p and V_s with respect to the initial wavespeed model are both substantial but they importantly differ. V_p presents variations up to 10%, while V_s variations reach 30% and the structural pattern is illuminated with several new details.

This different behavior may be explained considering that the initial *Im00* V_p model already resolves some strong structural features at the considered frequencies, while V_s is poorly imaged in *Im00*. Nonetheless, this means that in many areas V_p *Im25* is mostly inherited from *Im00*, which is based on a traveltime tomography. These considerations suggest interpreting the V_p/V_s *Im25* values with caution since artifacts could be present[57].

Discussion

The role of CO_2 in the Apennines. The sections across the northern, central, and southern Apennines (CC', DD', and EE') are relevant for studies of deep fluid circulation, in particular CO_2 that is responsible for degassing regions and induced seismicity in Italy[53].

Section CC' (Fig. 2) is a SW-NE cut from Monte Argentario to the Adriatic coast. Here *Im00* already imaged the high V_p wavespeeds of the Adriatic and Tyrrhenian plates and the low wavespeed to the SW (from ~50 to 90 km) related to the asthenospheric wedge beneath the Tuscany area. The *Im25* V_s model shows a body of relatively low wavespeed between 70 and 120 km along the section below 20 km depth. This corresponds to V_p/V_s values as high as 1.9–2.1, that can be associated to the asthenosphere and its thermal effect on the subducting Adriatic lower crust and upper mantle. According to[58], the geochemistry of the magmas in this region (Tuscan-Roman magmatic provinces) suggests they are related to melting of a mantle source that is metasomatized by subducted crustal material. Hence, the Tuscan-Roman Degassing Structure—TRDS—would reflect the degassing process of this metasomatized uprising mantle and would represent areas with an anomalous flux of deeply derived CO_2[58]. This corresponds to the high V_p/V_s values (expected for high temperature and partially melted rocks[59]; and references therein) retrieved in *Im25* for the Tuscany area below 20 km, as also evidenced by the close-up of section CC' (Fig. 2).

Beneath the Apennines belt (distances from 125 to 150 km) we find a volume of V_p/V_s as low as 1.6–1.65 at shallow depths. These values are consistent with those expected for rocks filled with pressurized CO_2[60,61] between ~6 and 20 km depth[23]. This agrees with a sudden disappearance of anomalous CO_2 flux and with gas accumulation in crustal traps at depth (fed by mantle derived CO_2)[58], generating CO_2 overpressurized reservoirs and inducing seismicity (e.g.,[62,63]). Following the above interpretation, we offer some speculative inferences about the low V_s and corresponding
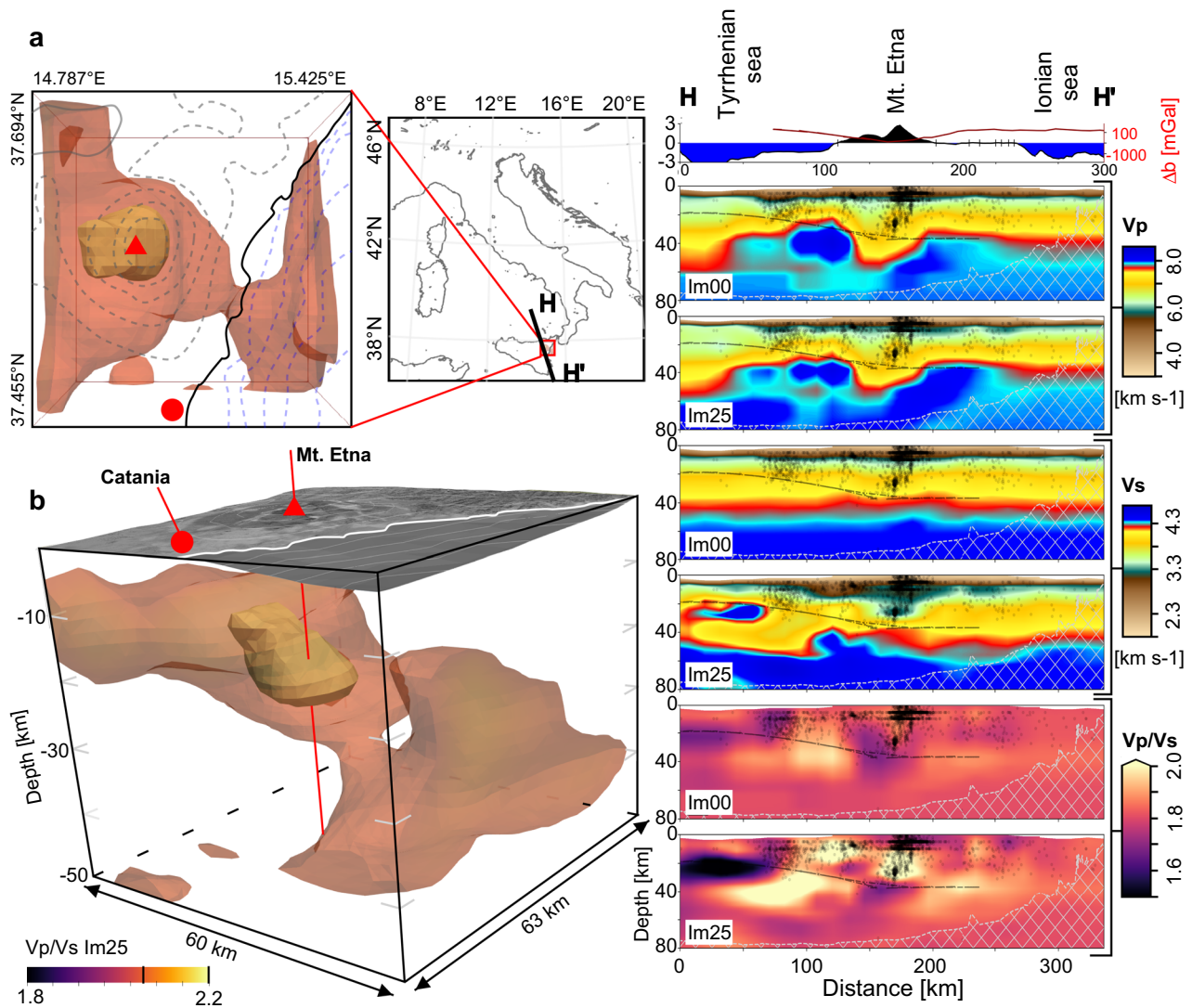
Fig. 3 Vertical cross-sections of models *Im00* and *Im25* for section HH' and 3D visualization of *Im25* V_p/V_s structure under Mt. Etna volcano. The cross-sections are a continuation of Fig. 2 showing section HH' of Figs. 1b, c. The sub-figures **a, b** show a close-up of the area around Mt. Etna volcano (red triangle) in a block of 60 km x 63 km and 50 km depth. In (**a**) the block is seen from the top and in (**b**) in a 3D view; black segment in the map is the trace of the section on the right; black or white lines denote the Sicilian coast in the two sub-figures, respectively. Isovolumes represent the V_p/V_s *Im25* model inside the block with orange denoting $V_p/V_s = 1.95$ and dark yellow denoting $V_p/V_s = 2.2$. A shallow, high V_p/V_s feature (2.2) is imaged right below the volcano and another high V_p/V_s isovolume (1.95) deepens southeastward below the Malta Escarpment.

high V_p/V_s values featured at distances from 150 to 200 km. These could represent a thermal effect of the flexure of the cold Adriatic lithosphere and another deep source of gas. Guided by the Alto Tiberina Fault that acts as a seal[61,63], the gas could contribute to the overpressurized reservoirs, but it could also move to the northeast, following the deep and ancient thrusts of the Adriatic lithosphere[64], possibly contributing to the presence of thermogenic gas in this area[65].

Section DD' (Fig. 2) is a SW-NE cut through the central Apennines from the Tyrrhenian to the Adriatic coast. In *Im25* the V_p/V_s ratio shows a contrast in the central part of the cross-section, with values ≥2 above 20 km depth, where earthquakes are concentrated[23]. Conversely, the deepest volume shows lower values, near 1.5, and a wide low P-wavespeed anomaly (~6 km s^{-1}) interpreted as the top of a regional thermal anomaly[66,67]. The anomaly is associated with a magmatic intrusion within the basement and coincides with an area characterized at the surface by anomalously high heat flux and high CO_2 fluxes from a deep

source[67]. The anomalous low V_p/V_s values are continuous down to depths of 35–40 km and can be considered, following[53], as a deep CO_2 storage zone that feeds the overlying aquifers. A correlation between deeply-derived CO_2 emissions and earthquake occurrence in the Apennines has been recently presented[53].

In section EE' (Fig. 2), below 30 km depth, *Im25* is better able to depict the fragmentation of the Adriatic lithosphere in terms of physical properties. The 50-km-wide low V_p anomaly close to the Tyrrhenian coast and deeper undulations of low V_s highlight the subduction of the Adriatic lithosphere and the Tyrrhenian asthenospheric wedge. The V_p/V_s model shows strong heterogeneities, with values above 1.9 from beneath the Tyrrhenian coast to below the belt and then beneath the Gargano promontory. On the Tyrrhenian side, such high values correspond to very low V_s values located just beneath Vesuvius at depth. This region hosts the Campanian volcanic province[58] characterized by high CO_2 flux induced by a deep source (CDS in Fig. 2) that we again coherently image as a high V_p/V_s area (Fig. 2).
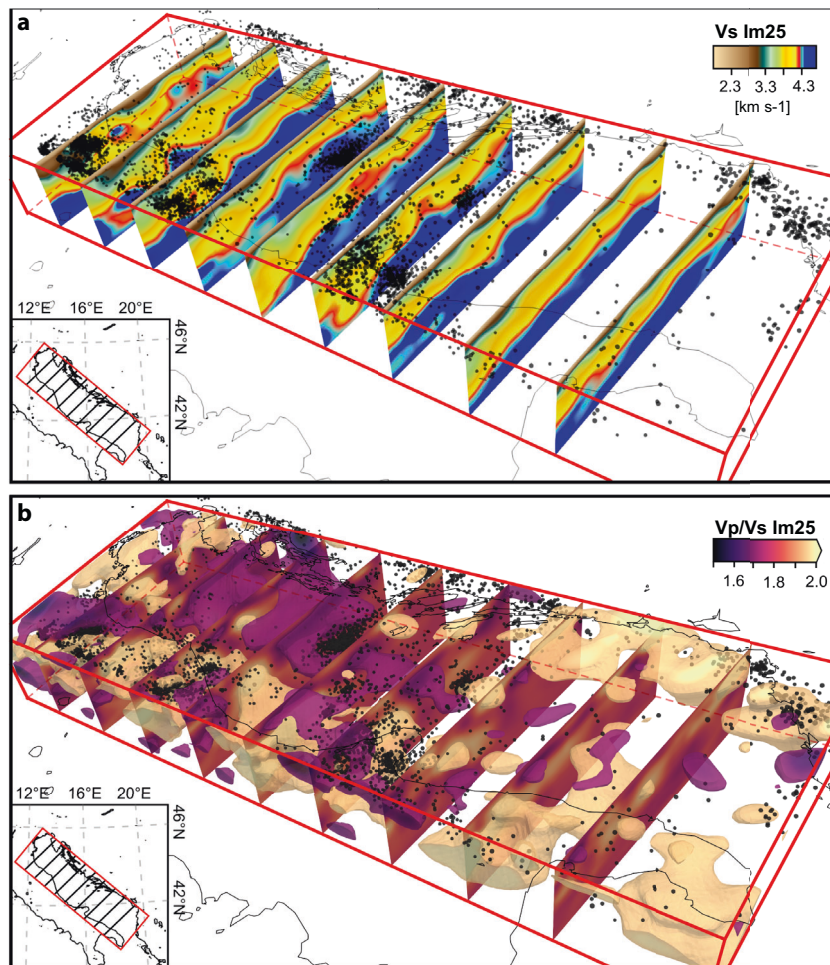
Fig. 4 Cross-sections through the Adriatic Sea for *Im25*. The nine slices, visualized in 3D, are oriented SW-NE through the Adriatic plate and show model *Im25* for V_s (**a**) and V_p/V_s (**b**). Inset map shows cross-section locations. Black dots represent the seismicity with locations from the INGV bulletin[85]. The slices are 260 km long and 80 km deep; coastlines are plotted on top of the slices. In (**b**), the purple and yellow isovolumes correspond to V_p/V_s values of 1.7 and 1.95.

Mt. Etna. West of the Calabrian Arc, *Im25* provides reliable images (Supplementary Fig. 12) that improve our understanding of the Italian lithospheric system. We introduce section HH' (Fig. 3), which is oriented NNW-SSE, parallel to the Tindari-Letojanni lithospheric alignment, and crossing the Mt. Etna volcanic complex, which was previously resolved down to depths shallower than ~30 km[22,54,68–71]. In the V_p model, we find a high wavespeed body (~6–7 km s^{-1}) from 6 km depth that is interpreted (following[68,69]) as a solidified intrusive body having a NNW-SSE horizontal axis and filled with magma feeding the shallower chamber above 5 km depth. These interpretations are also supported by recent petrological studies (e.g.,[55], and references therein) and shallow high-resolution tomography[54].

The region beneath Mt. Etna reveals a high V_p/V_s ratio (1.9–2.2) from 12 to 35 km depth, mainly caused by a deepening low V_s body. This imaged body could extend previous reconstructions of Mt. Etna plumbing system[69,70]. It is interpreted as the hypothesized[56] deep magmatic chamber below the Malta Escarpment (at ~30 km depth), which might be the source of magma intruding the solidified high V_p body[69] (see the 3D close-up in Fig. 3).

Breaking the Adriatic plate. The Adriatic plate has a debated structure ([6–8], and references therein) and plays a key role in the geodynamics of the western Mediterranean because of its location

between two major plates: Europe and Africa (Fig. 1). During the Cenozoic, the Adriatic plate was involved in the Apennines, Alpine, and Dinarides subduction zones, which surround its western, northern, and eastern margins, respectively.

The Adriatic plate east of the Italian coast is among the offshore zones where model *Im25* offers improved resolution with respect to previous tomographic models (e.g.,[9–14]). These previous models provided hints of the heterogeneities at a scale too large to support interpretations of local features. Conversely, geophysical studies associated with hydrocarbon extraction give very small scale images of the Adriatic plate, but only in some zones and at upper crustal depths (depth ≤10 km e.g.,[8]).

Our V_p and V_s *Im25* model investigates the structure almost continuously from north to south and from upper crust to upper mantle at a regional scale, showing lateral variations at both lower crust and upper mantle depths, which represent the different effects of the subduction process on the flexed downgoing Adriatic lithosphere. *Im25* exhibits features that motivate new interpretations for this complex area. We discuss these based on cross-sections aligned perpendicular and parallel to the Adriatic Sea axis (Figs. 4, 5, Supplementary Figs. 6, 8, and 10). These sections span a transitional area between two sectors of the Adriatic plate interpreted as microplates[6].

The portion north of the Gargano promontory, corresponding to the hypothesized northern microplate, shows vertical and
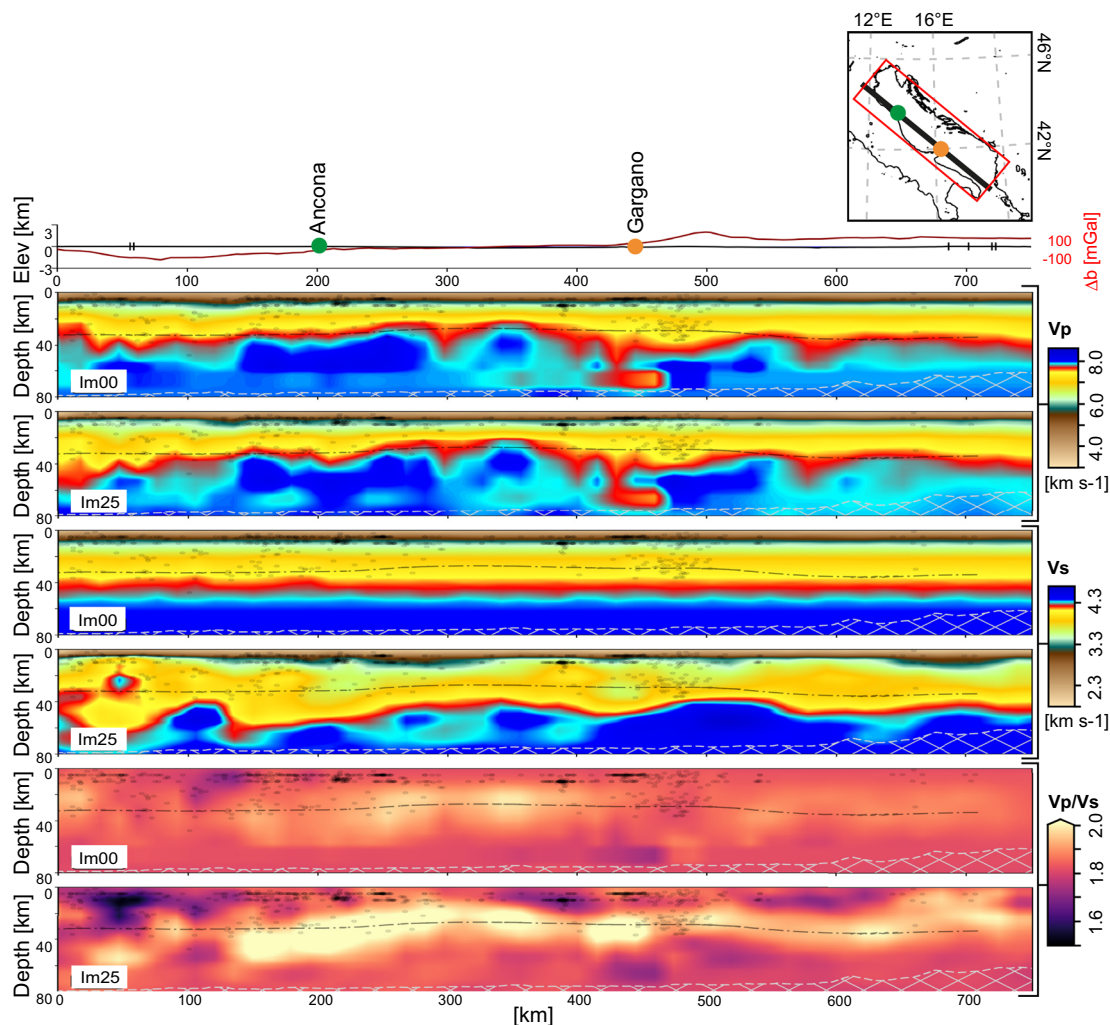
Fig. 5 Detailed vertical cross-section through the Adriatic Sea for *Im00* and *Im25*. The figure shows surface topography and Bouguer anomalies (top), and V_p, V_s, and the V_p/V_s ratio for models *Im00* and *Im25*. Dotted black lines in each section represent the Moho[29]. White dashed areas are not well-resolved in *Im25* model. Black dots represent relocated seismicity from the Italian Bulletin of INGV[85].

lateral heterogeneities that reflect the complex and long tectonic evolution of this area, beginning with Permian-Mesozoic rifting. The structure features the Adriatic plate that, within a restricted volume, subducts towards the Dinarides to the northeast, Eurasia to the north, and the Tyrrhenian plate to the southwest[7]. The six sections cutting through the Adriatic Sea above the Gargano promontory (Fig. 4) show complex undulations of wavespeeds. *Im25* exhibits a thickening of the Adriatic crust moving inland towards the southwest[15,30,31]. This can be considered evidence of the southwestward subduction of Adriatic lithosphere, now well-imaged also in V_s. In the sections south of Gargano, the steepness of the subducting Adriatic plate decreases, the wavespeed anomalies become suddenly smoother, and relatively low wavespeeds move deeper, indicating a thicker continental crust all along the southern portion of the plate. In the southern part, the layers are flatter, suggesting that the lithosphere is less affected by subduction. This is evident closer to the Italian coast, which, especially in V_s, shows an unmodified Adriatic lithosphere that is far enough away from both the Apennines and Dinarides fronts (Fig. 1a). Towards the northeast, the southern portion of the Adriatic lithosphere starts showing deeper undulations because the Adriatic plate progressively subducts under the Dinarides belt.

The three-dimensional structure in V_p/V_s can be displayed using isovolumes (Fig. 4b, Supplementary Fig. 10). We observe a change in V_p/V_s values at crustal depths (above 35 km). A low V_p/V_s ratio (≤1.7) body is found northwest of the Gargano promontory, while high V_p/V_s features (≤1.95) are found toward the southeast. This variation is probably due to lateral changes in the V_s model. The transition occurs near the deformation zone (Fig. 5). This area corresponds to a transition in the Bouguer anomaly from negative to positive values. Here the Moho is almost flat and several seismic sequences appear in the Adriatic offshore (black dots in Figs. 4, 5). These observations suggest that this is an unstable portion of the Adriatic plate, marking the separation between two distinct portions, either microplates or terranes[6].

Our model *Im25* highlights a northern portion of the Adriatic plate with more complex wavespeed anomalies and a thinner crust, and a southern part with a more regularly layered wavespeed structure and a thicker crust. The zone separating the two microplates—highlighted by earthquake occurrences and marked by a difference in stress regime—is now supported by full waveform tomographic images. Based on these evidences, our results corroborate the proposal[6,8] that the Adriatic plate consists of two distinct microplates, featuring different tectonic structures and dynamics.

Conclusions

Our tomographic model *Im25* for Italy has remarkable resolution for both V_p and V_s values compared to images from previous regional and continental models. It also compares favorably with local-scale, high-resolution tomographic models derived using different methodologies, and with studies from other geophysical fields. *Im25* illuminates the connections among the plates and microplates that feature the structure of the Italian lithosphere, including the under-thrusting of the Adriatic crust below the Tyrrhenian crust, the related asthenospheric wedge, and the boundary between the Tyrrhenian plate and the subducting Ionian plate.

Our tomographic model is consistent with the proposed distribution of fluids and melted materials in the Italian subsurface, which are also related to seismicity patterns. In the northern and southern Apennines, low V_s and high V_p/V_s anomalies in *Im25* are compatible with deep melted material that induces shallow CO_2 fluxes, and a low V_p/V_s volume beneath the northern Apennines belt is consistent with traps of overpressurized CO_2 inducing seismicity. Below the 2009 L'Aquila earthquake a low wavespeed body down to ~30 km depth, together with a low V_p/V_s volume within ~20–40 km depth, is interpreted as a deep CO_2 storage just beneath an area with dense seismicity and anomalously high heat flux and high CO_2 fluxes at the surface.

Model *Im25* illuminates Mt. Etna volcano, which had previously been investigated only at shallow depths. Our new images guide a better understanding of the volcano plumbing system: a ~30-km-deep anomaly with high V_p/V_s values appears to feed an intermediate-depth magma-filled intrusive body, which in turn is connected to a shallow chamber.

Our final model *Im25* provides reliable images of the Adriatic plate offshore area, which was only roughly outlined by previous regional and continental tomographic models. It supports the hypothesis, proposed by geodynamical studies, of a complex structure of the Adriatic plate made of two microplates that have distinct tectonic features and are differently affected by plate subduction. This provides a foundation for understanding the seismicity and stress regimes in the Adriatic region.

Methods

Dataset. We selected a total of 163 earthquakes that occurred in the chosen simulation volume between 2005 and 2014 and with a magnitude range 3.0–5.8 (red and blue dots in the inset of Fig. 1c). The initial source mechanisms are obtained from Time Domain Moment Tensor (TDMT) solutions that are routinely calculated by INGV[72] by inverting full, three-component traces of regional, broadband stations using 1D wavespeed models (http://terremoti.ingv.it/). The selection of the events and collection of the corresponding source parameters were done using the e-Science seismological gateway, i.e., the VERCE portal (European projects VERCE, www.verce.eu, and EPOS-IP, https://www.epos-ip.org).

The computational cost of an adjoint tomographic inversion scales with the number of events, i.e., two simulations are required for each earthquake, one forward and one adjoint[38,39], but is independent of the number of receivers. Therefore, we included all available stations of the Italian National Seismic Network (INSN), stations from local Italian permanent networks (i.e., the network in Basilicata, in NW and NE Italy, and in Irpinia), and also those of other European and Mediterranean networks located inside the simulation volume (i.e., GEOFON, MedNet, and Swiss, Greek, Hungarian, and Romanian networks), for a total of 412 stations (green triangles in the inset of Fig. 1c; see EIDA archive[73] https://eida.ingv.it). They are mainly three-component, broadband stations, densely but unevenly distributed along the peninsula (for more details see[37]), but not all of them recorded all events.

For each event the corresponding recorded seismograms were downloaded from the INGV EIDA/Orfeus archive, and a preliminary data quality check was performed by discarding traces with gaps or low (<3) signal-to-noise ratio. We used only velocity traces recorded by permanent stations (see EIDA archive[73] https://eida.ingv.it). Data recorded by temporary networks were neglected because these are short period (high frequency) instruments; these data could be useful for successive studies at higher resolution.

Initial model and parameterization. The geographical volume considered for the tomographic inversion covers the entire Italian peninsula and neighboring areas in France to the west, in Switzerland and Austria to the north, and along the eastern Adriatic coast and Greece to the east (Fig. 1). To simulate seismic wavefields with the SPECFEM3D_Cartesian spectral-element solver (Section "Forward and inverse modeling"), the geographical volume is discretized by a mesh of hexahedral elements with a total length of ~1204 km (from 36.11° to 47° of latitude), width of ~1250 km (from 6.5° to 21° of longitude), and depth of 80 km, thereby including both crust and upper mantle.

The starting model in our inversion procedure is a 3D tomographic P- and S-wavespeed model of the Italian lithosphere[29]. This tomographic model used both local and teleseismic events and also modeled P- and S-seismic phases refracted at the Moho discontinuity. It confirmed the main structural features observed in previous models in the best-resolved parts of the inverted volume, and it showed more detailed images of the Adriatic-Tyrrhenian plate system and of the less resolved areas of previous V_p models. However, the resolution for V_s, and consequently for the V_p/V_s ratio, was relatively poor and limited to restricted areas of the peninsula and to shallow depths (down to ~38 km).

To implement the starting model, we interpolate the wavespeed values (compressional wavespeed V_p and shear wavespeed V_s) of [29] at discrete points of the geometrical mesh. The same hexahedral model is used for successive iterations of the tomographic model. The density ρ is expressed as a quadratic function of V_p[74], $\rho = 0.025V_p^2 - 0.055V_p + 2.134$, where ρ is in g cm^{-3} and V_p in km s^{-1}. Thus, density changes during each iteration along with V_p. The quality factor Q, describing attenuation effects, is implemented as a linear function of V_s[75], $Q = 0.02V_s$, with V_s expressed in km s^{-1}.

In our inversion procedure, we parameterize the model using P- and S-wavespeed parameters since this could facilitate the direct implementation of the starting model[29] parameterized in the same way. This also favors the comparison with the results from other studies for Italy. However, this implies that we should be careful when considering and interpreting the obtained V_p/V_s values. In many areas, our V_p is inherited from the starting traveltime tomography which resolves P-wave features quite well. V_p may also have a different sensitivity with respect to V_s since P-waves have longer wavelengths compared to S-waves at the same period. Bulk-sound speed, which is independent from V_s, or radial anisotropy V_{sv} and V_{sh} parameters could be considered in future extensions of this work to improve the model through a more sensitive parameterization[48].

Source inversion. Before performing the tomographic inversion, we used the starting 3D wavespeed model and recalculated the source parameters of 123 events out of the 163 (red dots in the inset of Fig. 1c; see Section "Forward and inverse modeling"). We used the technique presented by [76] and implemented in their code *cmt3d_FLEXWIN*. The procedure requires an initial source solution for each event, which, in our case, is the TDMT solution based on a 1D wavespeed model and published in the INGV database (Section "Dataset"). SPECFEM3D_Cartesian (Section "Forward and inverse modeling") is used to simulate the synthetics for these source models and the starting 3D wavespeed structure, and to numerically calculate the Fréchet derivatives of a given waveform misfit function with respect to the source parameters. This misfit between data and synthetics is then minimized to invert for the six moment tensor components and the event location (a total of 9 source parameters).

Supplementary Fig. 13a shows the moment tensor solutions for each of the 123 events: the black beachball is the initial TDMT solution, the blue beachball is the solution of the source inversion performed using the starting 3D wavespeed structure (Supplementary Data 1). The 3D-based focal mechanisms are usually similar to the initial solutions. The variations in magnitude are generally low, as shown by the blue histogram in Supplementary Fig. 13b. The variations in depth are mostly around zero, but many events tend to be deeper when a 3D model is used (blue histogram in Supplementary Fig. 13c).

New forward simulations are performed for all the events using the new moment tensor solutions and the starting wavespeed model, thus establishing iteration *Im00*.

After producing the model *Im12* at iteration 12 (Section "Forward and inverse modeling"), we added 40 events (again described by TDMT source solutions) and performed a source inversion for the combined set of 163 events (red beachballs in Supplementary Fig. 13a; Supplementary Data 1). The procedure is the same as described before, but the underlying wavespeed model is now *Im12*. This second source inversion allows us to refine the source descriptions based on a wavespeed model that was iteratively improved through the first 12 tomographic iterations (orange histograms in Supplementary Figs. 13b, c).

Forward and inverse modeling. Wavefield simulations for both forward and inverse modeling in our study were performed using the software package *SPECFEM3D_Cartesian* ([50], https://github.com/geodynamics/specfem3d), which is based on the spectral-element method (SEM;[77,78]). The SEM combines exponential spatial accuracy due to a high-degree polynomial representation of the wavefield, computational efficiency guaranteed by an explicit time marching scheme easily implemented on parallel computers (e.g.,[50,79]), and geometrical flexibility. The solver *SPECFEM3D_Cartesian* is specifically designed for local and regional simulations and allows us to accommodate all complexities that affect seismic wave propagation, such as topography, lateral wavespeed variations, attenuation, anisotropy, absorbing conditions at model boundaries. The software also enables

adjoint simulations and finite-frequency sensitivity kernels required for inverse modeling of both source and structure parameters[39,50].

The input needed by the code are models of seismic wavespeeds and of the earthquake source. The simulated volume is discretized using a conformal, anisotropic, hexahedral mesh. In this study we use the mesh introduced in Section "Initial model and parameterization" with values of the material properties assigned to its nodes. The mesh has a total of 0.7 million of hexahedral elements with ~5 km sides at the mesh top and one tripling of element size in depth. Our mesh honors surface topography derived from the GEBCO_2014 grid (https://www.gebco.net/data_and_products/historical_data_sets/#gebco_2014), but it does not honor the Moho discontinuity. A preliminary study showed that the minimum numerical period resolved by this mesh is ~10 s (see Supplementary Fig. 14).

The adjoint inversion procedure is based on the definition of a misfit function that measures discrepancies between observed seismograms and corresponding synthetic seismograms. The initial wavespeed model is iteratively updated in order to minimize this misfit function and to better image structural heterogeneities in the region of interest. In the adjoint technique the variation of the misfit function can be written in terms of so-called misfit kernels[39] which are Fréchet derivatives of the misfit function with respect to the model parameters. These volumetric kernels reveal where the model is inadequate and should be updated in order to reduce the seismogram misfits.

The main advantage of the adjoint procedure is that to construct the misfit kernels it is not necessary to calculate all the single phase-specific kernels for each misfit measurement, which would require tens of thousands of wavefield simulations and therefore would be computationally unfeasible. Instead, one calculates so-called event kernels for each earthquake, based on the interaction between the forward wavefield and the corresponding adjoint wavefield. The adjoint wavefield is obtained by considering the adjoint sources at all the stations for a given event as simultaneous sources. Then, by summing the event kernels for all earthquakes, the overall misfit kernel is obtained[39].

Following this theory and the examples of previous studies in the field (e.g.,[9,41,48,49]), the structure of our tomographic inversion for Italy consists of successive iterations, each including the steps described below:

(i) For each selected event, the forward wavefield is simulated using *SPECFEM3D_Cartesian* and the wavespeed model at iteration *n*. The wavefield is saved as synthetic seismograms at the chosen stations. For the first 12 iterations we used 123 events (red dots in the inset of Fig. 1c) out of the 163 discussed in Section "Dataset". We added the remaining 40 events (blue dots in the inset of Fig. 1c) to the dataset at iteration 13. Most of these events have lower magnitudes and can be useful to constrain higher-frequency features of the model. They also improve the spatial coverage for the adjoint tomography. For iterations 19 to 25 we removed 34 events located in the eastern part of the Adriatic Sea. This allows us to focus on resolving the volume under the Italian peninsula by reducing possible artifacts due to the inclusion of waves traveling through the Adriatic Sea and of earthquakes with large azimuthal gaps. Removing events also reduces the computational costs for the last iterations.

(ii) The synthetic seismograms and corresponding observed seismograms are processed in the same way, by removing the trend and mean, tapering the waveforms, deconvolving the instrument response from the data, and bandpass filtering. We initially considered the period range 10–100 s also based on the minimum resolved period of the mesh; then at iteration 16 we shifted to periods of 10–40 s to emphasize body-wave sensitivity over surface waves.

(iii) Observed and simulated seismograms are compared using the code *FLEXWIN*[80], which, based on specific tuning parameters, automatically selects time windows on waveforms where data and synthetics have quantifiable agreement and good signal-to-noise ratio. These windows are suitable for misfit measurements and are the only windows considered in the next steps of the tomographic inversion.

(iv) Misfit measurements between data and synthetics are calculated within each window using the code *measure_adj*[41], which also calculates the corresponding adjoint sources based on the seismogram measurements. To quantify the discrepancy between data and synthetics, we performed multi-taper traveltime measurements:

$$\Delta\tau_i(\omega, \mathbf{m}) = \tau_i^{\mathrm{obs}}(\omega) - \tau_i(\omega, \mathbf{m}) \qquad (1)$$

where **m** is the given wavespeed model and τ_i^{obs} and τ_i are the frequency-dependent traveltimes for observed and synthetic waveforms in the ith time window.

(v) All the adjoint sources for each earthquake are considered as simultaneous sources located at the receivers. These adjoint sources generate the adjoint field of that event simulated using *SPECFEM3D_Cartesian* and the wavespeed model of iteration *n*. From the interaction between the forward and adjoint wavefields, the code constructs finite-frequency sensitivity kernels for each event and for the model parameters V_p and V_s, namely the isotropic event kernels K_α and K_β.

(vi) The misfit kernels for each model parameter at a given iteration are calculated by summing the corresponding event kernels over all the considered earthquakes. The misfit kernel represents the gradient of the misfit function[39].

(vii) Regularization is applied to the misfit kernels before using them for a model update. We first applied preconditioning. The approximate Hessian kernels, calculated simultaneously for all event kernels, are summed over all the events to obtain a positive, symmetric function to precondition the misfit kernel ([48,81]; see Supplementary Fig. 12). Preconditioning is needed to reduce high amplitudes of kernels around sources and receivers and to increase convergence of the minimization algorithm. Next a Gaussian smoothing is applied to the preconditioned misfit kernels by convolving them with a 3D Gaussian function[82]. The smoothing operation removes artifacts due to the presence of short-wavelength unresolved features in the model.

(viii) At each iteration a step length test is performed to define the size of the model perturbation. The next iteration model $n + 1$ is obtained by updating the current model n with a chosen percentage α of the misfit function gradient:

$$\mathbf{m}^{n+1} = \mathbf{m}^n + \alpha\mathbf{p}^n \qquad (2)$$

where the steepest descent vector **p** at the nth iteration is equal to minus the gradient **g** at n^{th} iteration, in turn obtained from the misfit kernels[39,82].

We performed a total of 25 tomographic iterations, in addition to 2 iterations of seismic source inversion (Section "Source inversion"), resulting in model *Im25* (Supplementary Data 2).

Considering equation (1), the corresponding multi-taper traveltime misfit function for a single window *i* used in this work is defined as follows[41]:

$$F_i(\mathbf{m}) = \frac{1}{H_i} \int_{-\infty}^{\infty} h_i(\omega)[(\tau_i^{\mathrm{obs}}(\omega) - \tau_i(\omega, \mathbf{m}))/\sigma_i(\omega)]^2 \, d\omega, \qquad (3)$$

where $\sigma_i(\omega)$ is the associated frequency-dependent uncertainty, $h_i(\omega)$ denotes a windowing function in the frequency domain, and H_i is the corresponding normalization factor. We apply equation (3) for each time window selected on a pair of observed and synthetic seismograms and then we sum over all *N* time windows to obtain the total misfit function *F*:

$$F = \frac{1}{N} \sum_{i=1}^{N} F_i. \qquad (4)$$

The trend of the total misfit function (i.e., summed over all the measurement windows) is summarized in Supplementary Fig. 1a.

The tomographic inversion requires thousands of 3D wavefield simulations, which requires major computational resources, in terms of memory and CPU-time. We used the European Tier-0 system GENCI/TGCC CURIE. On this machine, a forward simulation of 5-min seismograms for one event requires ~5 hours on 150 cores, i.e., ~750 CPU-hours. The simulations for all the 163 events were performed simultaneously on 24,450 cores, i.e., ~125,000 CPU-hours. The compute time for an adjoint simulation for one event is approximately three times the time of one forward simulation. For a complete iteration ~34 hours are required, i.e., ~850,000 CPU-hours. To perform the 25 tomographic iterations and 2 source inversions (described in Section "Source inversion"), a total of 36 million CPU-hours was used.

The computational resources have been obtained by the project IMAGINE_IT (PI Dimitri Komatitsch) during the 2014 9th PRACE call.

Resolution analyses. Our geological and geophysical interpretation of iteration 25 is supported by an assessment of the resolution of our model. In principle, individual resolution tests would have the same computational requirements as the main inversion[82]. Alternatively, using much less computation, several recent studies (e.g.,[16,48,49,83,84]) have calculated the approximate Hessian as a proxy of ray density and have performed point spread function (PSF) tests to assess local resolution in the final model. This is the approach followed in this study.

As reported in Section "Forward and inverse modeling", we calculated the approximate Hessian as a kernel pre-conditioner. Because of its sensitivity to amplitude effects due to wavefield geometrical spreading, the approximate Hessian is also adopted as a proxy for data coverage, illuminating the parts of the model that are well-resolved. In Supplementary Fig. 12 we hatch the regions with preconditioner values under a predefined threshold, focusing on the areas with good data density. According to [81], the data density map is an excellent indicator of resolution.

We performed PSF tests[83] in a few locations of interest, following e.g.,[9,16,36,49,84]. The PSF test consists of assessing the action of the Hessian on a local perturbation of the model by evaluating the degree of 'blurring' and distortion of that perturbation in the recovered model as well as the tradeoffs among model parameters. The computational cost is feasible since we only have to calculate the Fréchet derivatives of the misfit function for the perturbed model that corresponds to the cost of one adjoint iteration. We show in Supplementary Fig. 15 three PSF tests performed for the *Im25* model: a–c) a 3% Gaussian spherical V_s perturbation located 25 km below the Aeolian Islands (Tyrrhenian Sea) with ~50 km diameter; d–f) a 3% Gaussian spherical V_s perturbation located 25 km below Amatrice (Rieti, Central Italy) with ~50 km diameter; g–i) a 3% Gaussian spherical V_s perturbation located 10 km below Amatrice with ~20 km diameter. A certain level of smearing is

visible in these V_s PSFs, especially in the horizontal cross-sections and for case d–f. In this last case we observe residual spreading related to the uneven station network geometry along the peninsula, while this is not evident in PSF g–i with the same location but smaller diameter, and in PSF a–c since the area is covered by a more circular station network. Nevertheless, all the PSFs show a negligible trade-off between V_s and V_p (Supplementary Figs. 15c, f, and i), and the perturbations are reconstructed with adequate quality, suggesting that we can be confident in interpretations of the revealed anomalies.

Data availability

Code availability

References

1. Malinverno, A. & Ryan, W. B. F. Extension in the Tyrrhenian Sea and shortening in the Apennines as result of arc migration driven by sinking of the lithosphere. *Tectonics.* **5**, 227–245 (1986).
2. Stampfli, G. & Borel, G. A plate tectonic model for the Paleozoic and Mesozoic constrained by dynamic plate boundaries and restored synthetic oceanic isochrons. *Earth Planet. Sci. Lett.* **196**, 17–33 (2002).
3. Faccenna, C. et al. Mantle dynamics in the Mediterranean. *Rev. Geophys.* **52**, 283–332 (2014).
4. Molinari, I., Argnani, A., Morelli, A. & Basini, P. Development and testing of a 3D seismic velocity model of the Po Plain sedimentary basin, Italy. *Bull. Seismol. Soc. Am.* **105**, 753–764 (2015).
5. de Alteriis, G. Different foreland basins in Italy: examples from the central and southern Adriatic Sea. *Tectonophys.* **252**, 349–373 (1995).
6. D'Agostino, N. et al. Active tectonics of the Adriatic region from GPS and earthquake slip vectors. *J. Geophys. Res. Solid Earth.* **113**, 1–19 (2008).
7. Stampfli, G. Plate tectonic of the Apulia-Adria microcontinents. In Finetti, I. (ed.) CROP project - Deep seismic explorations of the central Mediterranean and Italy, 747–766 (Elsevier, 2005). http://www.geolsoc.org.uk/Plate-Tectonics/Chap4-Plate-Tectonics-of-the-UK/Variscan-Orogeny.
8. Scrocca, D., Carminati, E., Doglioni, C. & Marcantoni, D. Slab retreat and active shortening along the Central-Northern Apennines. In Lacombe, O., Roure, F., Lavé, J. & Vergés, J. (eds) Thrust Belts and Foreland Basins. Frontiers in Earth Sciences. (Springer, Berlin, Heidelberg, 2007).
9. Zhu, H., Bozdağ, E., Peter, D. & Tromp, J. Structure of the european upper mantle revealed by adjoint tomography. *Nat. Geosci.* **5**, 493–498 (2012).
10. Zhu, H., Bozdağ, E., Duffy, T. S. & Tromp, J. Seismic attenuation beneath Europe and the North Atlantic: implications for water in the mantle. *Earth Plane. Sci. Lett.* **381**, 1–11 (2013).
11. Fichtner, A. et al. Multiscale full waveform inversion. *Geophys. J. Int.* **194**, 534–556 (2013).
12. Blom, N., Gokhberg, A. & Fichtner, A. Seismic waveform tomography of the central and eastern Mediterranean upper mantle. *Solid Earth* **11**, 669–690 (2020).
13. Piromallo, C. & Morelli, A. P wave tomography of the mantle under the Alpine-Mediterranean area. *J. Geophys. Res. Solid Earth* **108**, 1–23 (2003).
14. Boschi, L., Ekström, G. & Kustowski, B. Multiple resolution surface wave tomography: the Mediterranean basin. *Geophys J. Int.* **157**, 293–304 (2004).
15. Gualtieri, L., Serretti, P. & Morelli, A. Finite-difference P wave travel time seismic tomography of the crust and uppermost mantle in the Italian region. *Geoche. Geophy. Geosyst.* **15**, 69–88 (2014).
16. Zhu, H. & Tromp, J. Mapping tectonic deformation in the crust and upper mantle beneath Europe and the North Atlantic Ocean. *Science.* **341**, 871–875 (2013).
17. Manu-Marfo, D., Aoudia, A., Pachhai, S. & Kherchouche, R. 3D shear wave velocity model of the crust and uppermost mantle beneath the Tyrrhenian basin and margins. *Sci. Reports.* **9**, 1–10 (2019).
18. Calò, M., Dorbath, C., Luzio, D., Rotolo, S. G. & D'Anna, G. Seismic velocity structures of southern Italy from tomographic imaging of the Ionian slab and petrological inferences. *Geophys. J. In.* **191**, 751–764 (2012).
19. Improta, L., De Gori, P. & Chiarabba, C. New insights into crustal structure, Cenozoic magmatism, CO_2 degassing, and seismogenesis in the southern Apennines and Irpinia region from local earthquake tomography. *J. Geophys. Res. Solid Earth.* **119**, 8283–8311 (2014).
20. Improta, L. et al. Reservoir structure and wastewater-induced seismicity at the Val d'Agri oilfield (Italy) shown by three-dimensional V_p and V_p/V_s local earthquake tomography. *J. Geophys. Res. Solid Earth* **122**, 9050–9082 (2017).
21. Baccheschi, P., Gori, P. D., Villani, F., Trippetta, F. & Chiarabba, C. The preparatory phase of the mw 6.1 2009 l'Aquila (Italy) normal faulting earthquake traced by foreshock time-lapse tomography. *Geol.* **48**, 49–55 (2020).
22. Patanè, D., Barberi, G., Cocina, O., De Gori, P. & Chiarabba, C. Time-resolved seismic tomography detects magma intrusions at mount Etna. *Science.* **313**, 821–823 (2006).
23. Chiarabba, C., Buttinelli, M., Cattaneo, M. & De Gori, P. Large earthquakes driven by fluid overpressure: the Apennines normal faulting system case. *Tectonics.* **39**, e2019TC006014 (2020).
24. Lippitsch, R., Kissling, E. & Ansorge, J. Upper mantle structure beneath the Alpine orogen from high-resolution teleseismic tomography. *J. Geophys. Res.* **108**, 2376 (2003).
25. Panza, G. F., Raykova, R. B., Carminati, E. & Doglioni, C. Upper mantle flow in the western Mediterranean. *Earth Planet. Sci. Lett.* **257**, 200–214 (2007).
26. Boschi, L., Fry, B., Ekström, G. & Giardini, D. The European upper mantle as seen by surface waves. *Surv. Geophys.* **30**, 463–501 (2009).
27. Verbeke, J., Boschi, L., Stehly, L., Kissling, E. & Michelini, A. High-resolution rayleigh-wave velocity maps of central Europe from a dense ambient-noise data set. *Geophys. J. Int.* **188**, 1173–1187 (2012).
28. Giacomuzzi, G., Civalleri, M., De Gori, P. & Chiarabba, C. A 3D Vs model of the upper mantle beneath Italy: insight on the geodynamics of central Mediterranean. *Earth Planet. Sci. Lett.* **335–336**, 105–120 (2012).
29. Di Stefano, R. & Ciaccio, M. G. The lithosphere and asthenosphere system in Italy as inferred from the Vp and Vs 3D velocity model and Moho map. *J. Geodyn.* **82**, 16–25 (2014).
30. Li, H., Bernardi, F. & Michelini, A. Surface wave dispersion measurements from ambient seismic noise analysis in Italy. *Geophys. J. Int.* **180**, 1242–1252 (2010a).
31. Li, H., Bernardi, F. & Michelini, A. Love wave tomography in Italy from seismic ambient noise. *Earthq. Sci.* **23**, 487–495 (2010b).
32. Molinari, I., Verbeke, J., Boschi, L., Kissling, E. & Morelli, A. Italian and Alpine three-dimensional crustal structure imaged by ambient-noise surface-wave dispersion. *Geochem. Geophys. Geosyst.* **16**, 4405–4421 (2015).
33. Kästle, E. D. et al. Surface Wave Tomography of the Alps Using Ambient-Noise and Earthquake Phase Velocity Measurements. *J. Geophys. Res. Solid Earth.* **123**, 1770–1792 (2018).
34. Zhao, L. et al. Evidence for a serpentinized plate interface favouring continental subduction. *Nat. Commun.* **11**, 2171 (2020).
35. Lu, Y., Stehly, L., Brossier, R., Paul, A. & Group, A. W. Imaging Alpine crust using ambient noise wave-equation tomography. *Geophys. J. Int.* **222**, 69–85 (2020).
36. Zhu, H., Bozdağ, E. & Tromp, J. Seismic structure of the European upper mantle based on adjoint tomography. *Geophys. J. Int.* **201**, 18–52 (2015).
37. Michelini, A. et al. The Italian National Seismic Network and the earthquake and tsunami monitoring and surveillance systems. *Adv. Geosci.* **43**, 31–38 (2016).
38. Tromp, J. Seismic wavefield imaging of Earth's interior across scales. *Nat. Rev. Earth & Environment.* **1**, 40–53 (2020).
39. Tromp, J., Tape, C. & Liu, Q. Seismic tomography, adjoint methods, time reversal and banana-doughnut kernels. *Geophys. J. Int.* **160**, 195–216 (2005).
40. Plessix, R. E. A review of the adjoint-state method for computing the gradient of a functional with geophysical applications. *Geophys. J. Int.* **167**, 495–503 (2006).
41. Tape, C., Liu, Q., Maggi, A. & Tromp, J. Adjoint tomography of the southern California crust. *Science.* **325**, 988–992 (2009).
42. Fichtner, A., Kennett, B. L. N., Igel, H. & Bunge, H.-P. Full seismic waveform tomography for upper-mantle structure in the Australasian region using adjoint methods. *Geophys. J. Int.* **179**, 1703–1725 (2009).
43. Fichtner, A., Kennett, B. L., Igel, H. & Bunge, H. P. Full waveform tomography for radially anisotropic structure: New insights into present and past states of the Australasian upper mantle. *Earth Planet. Sci. Lett.* **290**, 270–280 (2010).
44. Chen, M. et al. Lithospheric foundering and underthrusting imaged beneath Tibet. *Nat. Commun.* **8**, 1–10 (2017).

45. Krischer, L., Fichtner, A., Boehm, C. & Igel, H. Automated large-scale full seismic waveform inversion for North America and the North Atlantic. *J. Geophys. Res.* **123**, 5902–5928 (2018).

46. Zhu, H., Stern, R. J. & Yang, J. Seismic evidence for subduction-induced mantle flows underneath Middle America. *Nat. Commun.* **11**, 2075 (2020).

47. Baron, J. & Morelli, A. Full-waveform seismic tomography of the Vrancea, Romania, subduction region. *Phys. Earth Planet. Interiors* **273**, 36–49 (2017).

48. Bozdağ, E. et al. Global adjoint tomography: First-generation model. *Geophys. J. Int.* **207**, 1739–1766 (2016).

49. Lei, W. et al. Global adjoint tomography – Model GLAD-M25. *Geophys. J. Int.* **223**, 1–21 (2020).

50. Peter, D. et al. Forward and adjoint simulations of seismic wave propagation on fully unstructured hexahedral meshes. *Geophys. J. Int.* **186**, 721–739 (2011).

51. Casarotti, E. et al. Fast 3D seismic wave simulations of 24 august 2016 M_w 6.0 central Italy earthquake for visual communication. *Annals of Geophys.* **59**, 1–7 (2016).

52. Diaferia, G. et al. Inferring Crustal Temperatures Beneath Italy From Joint Inversion of Receiver Functions and Surface Waves. *J. Geophys. Res. Solid Earth Mediterr. Region.* **124**, 8771–8785 (2019).

53. Chiodini, G. et al. Correlation between tectonic CO_2 Earth degassing and seismicity is revealed by a 10-year record in the Apennines, Italy. *Sci. Adv.* **6**, eabc2938 (2020).

54. Giampiccolo, E., Cocina, O., De Gori, P. & Chiarabba, C. Dyke intrusion and stress-induced collapse of volcano flanks: The example of the 2018 event at Mt. Etna (Sicily, Italy). *Sci. Rep.* **10**, 1–8 (2020).

55. Di Renzo, V., Corsaro, R. A., Miraglia, L., Pompilio, M. & Civetta, L. Long and short-term magma differentiation at Mt. Etna as revealed by Sr-Nd isotopes and geochemical data. *Earth-Sci. Rev.* **190**, 112–130 (2019).

56. Neri, M., Rivalta, E., Maccaferri, F., Acocella, V. & Cirrincione, R. Etnean and Hyblean volcanism shifted away from the Malta Escarpment by crustal stresses. *Earth Planet. Sci. Lett.* **486**, 15–22 (2018).

57. Michelini, A. Testing the reliability of Vp/Vs anomalies in traveltime tomography. *Geophys. J. Int.* **114**, 405–410 (1993).

58. Chiodini, G. et al. Carbon dioxide earth degassing and seismogenesis in central and southern Italy. *Geophys. Res. Lett.* **31**, L07615 (2004).

59. Sanders, C. O., Ponko, S. C., Nixon, L. D. & Schwartz, E. A. Seismological evidence for magmatic and hydrothermal structure in Long Valley caldera from local earthquake attenuation and velocity tomography. *J. Geophys. Res.* **100**, 8311–8326 (1995).

60. Rojas, E. V_p-V_s ratio sensitivity to pressure, fluid, and lithology changes in tight gas sandstones. *First Break* **26**, 83–86 (2008).

61. Moretti, M., De Gori, P. & Chiarabba, C. Earthquake relocation and three-dimensional V_p and V_p/V_s models along the low angle Alto Tiberina Fault (Central Italy): Evidence for fluid overpressure. *Geophys. J. Int.* **176**, 833–846 (2009).

62. Miller, S. A. et al. Aftershocks driven by a high-pressure CO_2 source at depth. *Nature.* **427**, 724–727 (2004).

63. Valoroso, L., Chiaraluce, L., Di Stefano, R. & Monachesi, G. Mixed-mode slip behavior of the Altotiberina low-angle normal fault system (Northern Apennines, Italy) through high-resolution earthquake locations and repeating events. *J. Geophys. Res. Solid Earth* **122**, 10,220–10,240 (2017).

64. Barchi, M., Minelli, G., Magnani, B. & Mazzotti, A. Line CROP 03: Northern Apennines. *Mem. Descr. Carta Geol. d'It.* **LXII**, 127–136 (2003).

65. Carlin, S. & Dainelli, J. Pressure Regimes and Pressure Systems in the Adriatic Foredeep (Italy). In Law, B., Ulmishek, G. & Slavin, V. (eds) Abnormal pressures in hydrocarbon environments, chap. 9, 145–160 (American Association of Petroleum Geologists, 1998).

66. Chiarabba, C., Bagh, S., Bianchi, I., De Gori, P. & Barchi, M. Deep structural heterogeneities and the tectonic evolution of the Abruzzi region (Central Apennines, Italy) revealed by microseismicity, seismic tomography, and teleseismic receiver functions. *Earth Planet. Sci. Lett.* **295**, 462–476 (2010).

67. Chiodini, G., Cardellini, C., Caliro, S., Chiarabba, C. & Frondini, F. Advective heat transport associated with regional Earth degassing in central Apennine (Italy). *Earth Planet. Sci. Lett.* **373**, 65–74 (2013).

68. Aloisi, M., Cocina, O., Neri, G., Orecchio, B. & Privitera, E. Seismic tomography of the crust underneath the Etna volcano, Sicily. *Phys. Earth Planet. Interiors.* **134**, 139–155 (2002).

69. Patanè, D., De Gori, P., Chiarabba, C. & Bonaccorso, A. Magma ascent and the pressurization of Mount Etna's volcanic system. *Science.* **299**, 2061–2063 (2003).

70. Calò, M., Parisi, L. & Luzio, D. Lithospheric P- and S-wave velocity models of the Sicilian area using WAM tomography: Procedure and assessments. *Geophys. J. Int.* **195**, 625–649 (2013).

71. De Gori, P. et al. Re-pressurized magma at Mt. Etna, Italy, may feed eruptions for years. *Commu. Earth Environ.* **2**, https://doi.org/10.1038/s43247-021-00282-9 (2021).

72. Scognamiglio, L., Tinti, E. & Michelini, A. Real-time determination of seismic moment tensor for the Italian region. *Bull. Seismol. Soc. Am.* **99**, 2223–2242 (2009).

73. Danecek, P. et al. The Italian Node of the European Integrated Data Archive. *Seismol. Res. Lett.* **92**, 1726–1737 (2021).

74. Magnoni, F. et al. Spectral-element simulations of seismic waves generated by the 2009 L'Aquila earthquake. *Bull. Seismol. Soc. Am.* **104**, 73–94 (2014).

75. Olsen, K. B., Day, S. M. & Bradley, C. R. Estimation of Q for long-period (>2 sec) waves in the Los Angeles basin. *Bull. Seismol. Soc. Am.* **93**, 627–638 (2003).

76. Liu, Q., Polet, J., Komatitsch, D. & Tromp, J. Spectral-element moment tensor inversions for earthquakes in Southern California. *Bull. Seismol. Soc. Am.* **94**, 1748–1761 (2004).

77. Komatitsch, D. & Tromp, J. Introduction to the spectral-element method for 3-D seismic wave propagation. *Geophys. J. Int.* **139**, 806–822 (1999).

78. Chaljub, E. et al. Spectral element analysis in seismology. In Wu, R.-S. & Maupin, V. (eds) *Advances in wave propagation in heterogeneous media*, vol. 48 of *Advances in Geophysics*, 365–419 (Elsevier - Academic Press, London, UK, 2007).

79. Komatitsch, D. Fluid-solid coupling on a cluster of GPU graphics cards for seismic wave propagation. *C. R. Acad. Sci., Ser. IIb Mec.* **339**, 125–135 (2011).

80. Maggi, A., Tape, C., Chen, M., Chao, D. & Tromp, J. An automated time window selection algorithm for seismic tomography. *Geophys. J. Int.* **178**, 257–281 (2009).

81. Luo, Y., Modrak, R. & Tromp, J. Strategies in adjoint tomography. In Freeden, W., Nahed, Z. & Sonar, T. (eds) Handbook of Geomathematics (Springer, 2013), 2nd edn.

82. Tape, C., Liu, Q. & Tromp, J. Finite-frequency tomography using adjoint methods - Methodology and examples using membrane surface waves. *Geophys. J. Int.* **168**, 1105–1129 (2007).

83. Fichtner, A. & Trampert, J. Resolution analysis in full waveform inversion. *Geophys. J. Int.* **187**, 1604–1624 (2011).

84. Chen, M., Niu, F., Liu, Q., Tromp, J. & Zheng, X. Multiparameter adjoint tomography of the crust and upper mantle beneath East Asia: 1. Model construction and comparisons. *J. Geophys. Res. Solid Earth.* **120**, 1762–1786 (2015).

85. ISIDe Working Group. Italian seismological instrumental and parametric database (iside) http://iside.rm.ingv.it/ (2007).

86. DISS Working Group. Database of Individual Seismogenic Sources (DISS), Version 3.2.1: A compilation of potential sources for earthquakes larger than M 5.5 in Italy and surrounding areas http://diss.rm.ingv.it/diss/ (2018).

87. Šumanovac, F. Lithosphere structure at the contact of the Adriatic microplate and the Pannonian segment based on the gravity modelling. *Tectonophys.* **485**, 94–106 (2010).

88. Meghraoui, M. & Pondrelli, S. Active faulting and transpression tectonics along the plate boundary in North Africa. *Annals of Geophys.* **55**, 955–967 (2012).

Author contributions

F.M., E.C., & D.K. conceived the project. F.M. & E.C. collected and analyzed seismic data, and conducted the adjoint tomography. F.M. took the lead in writing the manuscript. D.K. added specific updates to the software package SPECFEM3D_Cartesian. J.T. & C.T. contributed to the theory of adjoint tomography. D.M. & D.K. managed the computational infrastructures. F.M., E.C., R.D.S., M.G.C., C.T., and J.T. co-wrote the manuscript. F.M., E.C., R.D.S. M.G.C., A.P., D.M., & A.M. contributed to the model interpretation. F.M., E.C., R.D.S., M.G.C., C.T., A.P., D.M., A.M., & J.T. reviewed the manuscript.

Competing interests

The authors declare no competing interests.

Additional information

Supplementary information The online version contains supplementary material available at https://doi.org/10.1038/s43247-022-00397-7.

Correspondence and requests for materials should be addressed to Federica Magnoni.

Peer review information *Communications Earth & Environment* thanks Lapo Boschi and the other, anonymous, reviewer(s) for their contribution to the peer review of this work. Primary Handling Editors: Luca Dal Zilio and Joe Aslin. Peer reviewer reports are available.

Reprints and permission information is available at http://www.nature.com/reprints

Publisher's note Springer Nature remains neutral with regard to jurisdictional claims in published maps and institutional affiliations.